Earth and Planetary Science Letters 381 (2013) 78–91

Contents lists available at ScienceDirect

Earth and Planetary Science Letters

www.elsevier.com/locate/epsl

The relationship between shear wave velocity, temperature, attenuation and viscosity in the shallow part of the mantle

Keith Priestley, Dan McKenzie *

Department of Earth Sciences, Bullard Labs, Madingley Road, Cambridge CB3 0EZ, UK

ARTICLE INFO

Article history:
Received 3 February 2013
Received in revised form 16 July 2013
Accepted 10 August 2013
Available online 25 September 2013
Editor: P. Shearer

Keywords:
surface wave tomography
mantle temperature
lithospheric thickness
shear wave attenuation
mantle viscosity

ABSTRACT

Surface wave tomography, using the fundamental Rayleigh wave velocities and those of higher modes between 1 and 4 and periods between 50 and 160 s, is used to image structures with a horizontal resolution of ~250 km and a vertical resolution of ~50 km to depths of ~300 km in the mantle. A new model, PM_v2_2012, obtained from 3×10^6 seismograms, agrees well with earlier lower resolution models. It is combined with temperature estimates from oceanic plate models and with pressure and temperature estimates from the mineral compositions of garnet peridotite nodules to generate a number of estimates of $SV(P,T)$ based on geophysical and petrological observations alone. These are then used to estimate the unrelaxed shear modulus and its derivatives with respect to pressure and temperature, which agree reasonably with values from laboratory experiments. At high temperatures relaxation occurs, causing the shear wave velocity to depend on frequency. This behaviour is parameterised using a viscosity to obtain a Maxwell relaxation time. The relaxation behaviour is described using a dimensionless frequency, which depends on an activation energy E and volume V_a. The values of E and V_a obtained from the geophysical models agree with those from laboratory experiments on high temperature creep. The resulting expressions are then used to determine the lithospheric thickness from the shear wave velocity variations. The resolution is improved by about a factor of two with respect to earlier models, and clearly resolves the thick lithosphere beneath active intracontinental belts that are now being shortened. The same expressions allow the three dimensional variations of the shear wave attenuation and viscosity to be estimated.

1. Introduction

The association of reduced shear wave velocity V_s, increased attenuation and reduced viscosity in the Earth's upper mantle has been known for almost ninety years (see Gutenberg, 1959, p. 76). These effects are most obvious in the asthenosphere, where the mantle temperature approaches the melting temperature. Fig. 1a shows a typical steady state continental geotherm. The layer close to the surface, where heat is transported by conduction alone, is known as the mechanical boundary layer (MBL). It is underlain by a thermal boundary layer (TBL) that forms part of the convective circulation of the upper mantle, and which supplies heat to the base of the MBL. At greater depths the temperature gradient in the convective interior is isentropic. No discontinuities in either the temperature or its gradient can occur anywhere. A convenient way to describe a geotherm is in terms of the equivalent lithospheric thickness, defined as the depth at which the extrapolated conductive geotherm would intersect that of the convective interior. This definition was used by Priestley and McKenzie (2006), hereafter PM6, and is also used here. It is then the same as the plate thickness used to parameterise the thermal structure of oceanic plates (see Crosby et al., 2006). As Fig. 1a shows, the base of the lithosphere defined in this way lies within the thermal boundary layer, and does not correspond to any physical boundary. Furthermore the temperature of that part of the thermal boundary layer that lies below the base of the lithosphere is lower than that of the isentropic interior. Figs. 1b–1e show two temperature profiles from western Africa and their best fitting geotherms, together with their SV profiles. There is no step in the velocity profiles corresponding to the base of the lithosphere.

A variety of other definitions of lithospheric thickness have been proposed. The original definition corresponded to what is now generally known as the elastic thickness (see Watts, 2001) and is now rarely used. Rychert and Shearer (2009) and Schmerr (2012) mapped SS precursors, which are generated by a drop in V_s of 5–10% across a boundary no more than 20 km thick at a depth of 35–120 km. This boundary they defined to be the lithosphere–asthenosphere boundary. The cause of the velocity decrease is uncertain. It could result from the presence of melt, a change in composition, or from anisotropy. But it is too sharp to be produced by temperature variations within a solid peridotite. There is

* Corresponding author. Tel.: +44 1223 337191.
E-mail address: mckenzie@madingley.org (D. McKenzie).

0012-821X/$ – see front matter
http://dx.doi.org/10.1016/j.epsl.2013.08.022

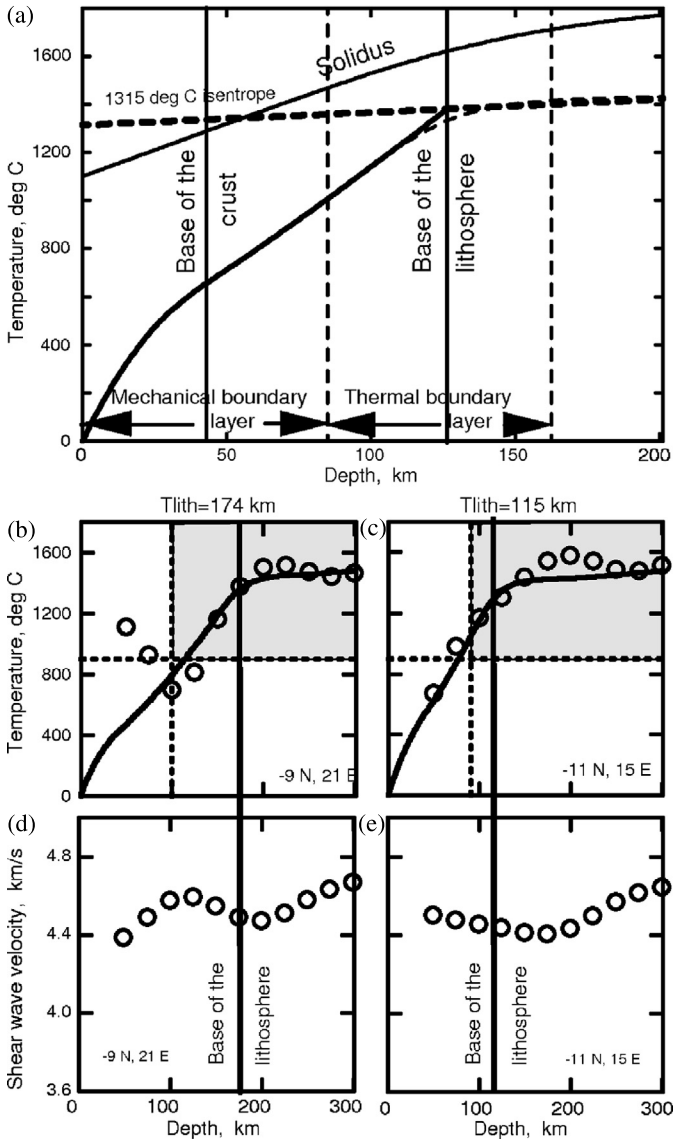

Fig. 1. (a) Sketch to show the model used to determine the lithospheric thickness. Heat transport in the mechanical boundary layer is entirely by conduction, and heat generated by radioactive decay in the crust causes the temperature gradient to decrease with depth. Heat transport within the thermal boundary layer changes from being conductive at its top to being convective at its base at 162 km. At greater depths the temperature gradient is isentropic with a potential temperature of 1315 °C. The base of the lithosphere is defined as the depth (126 km) at which the temperature on the conductive geothermal would have a potential temperature of 1315 °C. The geotherm that takes account of convection is shown as a thin dashed line, which only differs appreciably from the conductive profile, shown as the heavy solid line, near the base of the lithosphere. (b) and (c) show temperature estimates from PM_v2_2012 at two locations in western Africa. Only the estimates in the shaded regions are used to fit geotherms and hence determine the lithospheric thicknesses using the model in (a). The corresponding SV profiles are shown in (d) and (e).

therefore no obvious relationship between this definition of lithospheric thickness and that used here and illustrated in Fig. 1. Li et al. (2007) have used S-wave receiver functions to define the base of the lithosphere. Since conversions between S and P waves require large velocity gradients, there is no obvious relationship between their definition and that used here. Yuan and Romanowicz (2010) proposed yet another definition of lithospheric thickness, based on the vertical distribution of anisotropy. Their definition also has no obvious relationship to the one used here.

Though in principle V_s is controlled by the composition and temperature of the mantle, a number of studies (Jordan, 1979; Schutt and Lesher, 2006; Priestley and McKenzie, 2006) have concluded that change in V_s resulting from melt extraction from a garnet peridotite is small, and is unlikely to exceed 1%. Since the thick lithosphere beneath cratons is believed to be the residue of partial melting, variations in shear wave velocity within the upper part of the mantle are likely to result from variations in temperature, not composition. A number of laboratory experiments (Jackson, 2000; Gribb and Cooper, 1998) have shown that temperature variations can produce shear velocity variations of as large as 10–20%, even in the absence of melt. These results demonstrate that variations in V_s can be used to map three dimensional variations in the temperature of the uppermost mantle if the functional form of $V_s(T, P)$ can be determined. Two approaches to this problem have been used. Goes et al. (2000) and Faul and Jackson (2005) extrapolated the results from laboratory experiments to mantle conditions to estimate the temperature from the pressure and V_s. There are a number of problems with their approach. The dependence of V_s on temperature is a function of the grain size, and that used in laboratory experiments is at least two orders of magnitude smaller than that of the mantle. The problem would be less important if there was a good theoretical basis for the extrapolation, which sadly does not yet exist. Another problem is that the grain size of mantle peridotite is not well determined. That of mantle nodules is easily measured, but may have been affected by the deformation involved in their extraction from the mantle. These difficulties caused PM6 to use a different approach. They took a three dimensional mantle model of SV, determined from Rayleigh wave tomography, estimates of temperature from a thermal model of oceanic spreading centres, and pressure and temperature estimates from garnet peridotite nodules brought to the surface by magmas. They assumed that $SV = SV(P, T, a)$, where a is an activated process

$$a = \exp\left[-\left(\frac{E + PV_a}{RT}\right)\right] \tag{1}$$

E is the activation energy, V_a the activation volume, R the gas constant and T the absolute temperature. They then expanded SV using a Taylor expansion

$$SV = SV(P, T, 0) + \left(\frac{\partial SV}{\partial a}\right)a \tag{2}$$

They assumed the partial derivative, E and V_a were constant and determined their values from the geophysical and petrological observations. Their approach is empirical, and makes no assumptions about the nature of the activated process. They then fitted steady state geotherms to their estimates of $T(z)$. This approach makes no use of the laboratory data, and therefore avoids the problems associated with their extrapolation.

McCarthy et al. (2011) have recently taken a new approach to this problem. They scaled the frequency f of the seismic waves using the Maxwell time scale $\tau_M = \eta/\mu$, where $\eta = \eta(a)$ is the viscosity, a is given by Eq. (1), and $\mu(P, T)$ is the shear modulus, to give a dimensionless frequency f', where $f' = \tau_M f$. They then obtained expressions for $V_s = V_s(f')$ by fitting a variety of laboratory experiments with $1 \leqslant f' \leqslant 10^5$. They had no experimental constraints in the seismically important range $10^8 \leqslant f' \leqslant 10^{11}$. Their method also allows the attenuation Q_s^{-1} to be obtained. Their approach also provides estimates of η and hence of the grain size. It is therefore more powerful than either of the two earlier methods. Because it is in effect a special case of PM6's approach (see below), it is easily implemented in the same way as they did, by using a variety of geophysical and petrological data, including estimates of attenuation and mantle viscosity, to determine the relevant parameters. The analytic expressions are contained in Section 2, and the geophysical and petrological data used to estimate the parameters in Section 3. Section 4 compares the values of the parameters

obtained from the fitting process with those from laboratory experiments, and Section 5 discusses the results from applying the new approach to a new tomographic model.

2. Analytical expressions

McCarthy et al. (2011) define complex compliance $J^\star(f')$ using

$$J^\star(f') = J_1(f') + iJ_2(f') \tag{3}$$

where J_1 and J_2 are real functions of the dimensionless frequency f'. The shear velocity V_s and attenuation Q_s^{-1} are given by

$$V_s = 1/\sqrt{\rho J_1}, \qquad Q_s^{-1} = J_2/J_1 \tag{4}$$

and

$$f' = \tau_M f \tag{5}$$

where f is the frequency at which $J^\star$ is determined. The Maxwell relaxation time τ_M is

$$\tau_M = J_u(P,T)\eta \tag{6}$$

J_u is the unrelaxed compliance: that determined at high frequencies (typically MHz) where relaxation effects do not occur, and η is the viscosity, which can be written as

$$\eta = c/a \tag{7}$$

where a is the activation parameter given by Eq. (1) and c is a constant that depends on the grain size (diameter) d

$$c = \eta_1\left(\frac{d}{d_r}\right)^m \tag{8}$$

where η_1, d_r and m are constants. When the deformation occurs by Nabarro–Herring creep, involving body diffusion, $m = 2$, whereas if the creep mechanism is Coble creep, by grain boundary diffusion, $m = 3$. The unrelaxed compliance is related to the (real) shear modulus

$$J_u(P,T) = 1/\mu(P,T) \tag{9}$$

and μ can be expanded in a Taylor Series

$$\mu(P,T) = \mu(0,0) + \left(\frac{\partial\mu}{\partial T}\right)_0 T + \left(\frac{\partial\mu}{\partial P}\right)_0 P \tag{10}$$

McCarthy et al. (2011) write J_1 in terms of J_u and a function F of f'

$$J_1 = J_u/F(f') \tag{11}$$

where

$$F(f') = \begin{cases} \sum_{k=0}^{6} a_k(\ln f')^k, & f' \leqslant f'_r \\ 1, & f' > f'_r,\ f'_r = 10^{13} \end{cases} \tag{12}$$

and determine the seven empirical constants a_0 through a_6 from the laboratory experiments

$$a_0 = 0.55097, \qquad a_1 = 0.054332, \qquad a_2 = -0.0023616$$
$$a_3 = 5.7175\times10^{-5}, \qquad a_4 = 9.9473\times10^{-6}$$
$$a_5 = 3.4761\times10^{-7}, \qquad a_6 = 3.9461\times10^{-9}$$

They use the Kamers–Kronig relations to relate J_1 and J_2. These give (their Eqs. (18) and (25))

$$J_2 = J_u\left[\frac{\pi}{2}X_n(\tau') + \tau'\right], \quad \tau' = \frac{1}{2\pi f'} \tag{13}$$

where

$$X_n = 0.32(\tau')^y, \quad y = 0.39 - 0.28/\left(1 + 2.6\tau'^{0.1}\right),\ \tau' \geqslant 10^{-11}$$
$$= 1853\sqrt{\tau'}, \quad \tau' < 10^{-11} \tag{14}$$

When using these expressions it is convenient to avoid computational problems that occur when $\exp[(E + PV_a)/RT]$ becomes large by defining

$$\eta_0 = c\exp\left[(E + P_rV_a)/RT_r\right] \tag{15}$$

and

$$a^\star = \frac{\exp[(E + P_rV_a)/RT_r]}{\exp[(E + PV_a)/RT]} \tag{16}$$

when

$$\eta = c/a = \eta_0/a^\star \tag{17}$$

Clearly the value of η is not affected by the values chosen for P_r and T_r, which were 1.5 GPa and 1473 K ($\equiv$ 1200 °C). The values of the six parameters $\mu(0,0)$, $(\partial\mu/\partial T)_0$, $(\partial\mu/\partial P)_0$, η_0, E and V_a were determined by fitting the geophysical and petrological observations and are listed for various models in Table 1.

It is straightforward to relate McCarthy et al.'s expression for V_s to that used by PM6. Writing

$$f' = f'_0(1-\epsilon) \tag{18}$$

where f'_0 $(< 10^{13})$ is a reference frequency and $\epsilon \ll 1$, and expanding F in terms of ϵ gives

$$F(f') = F_1 - \epsilon F_2 + O(\epsilon^2) \tag{19}$$

where

$$F_1 = F(f'_0), \qquad F_2 = \sum_{k=1}^{6} ka_k(\ln f'_0)^k \tag{20}$$

Then

$$V_s(P,T,0) = \left(\frac{F_1}{\rho J_u}\right)^{1/2}\left[1 + \frac{F_2}{2F_1}\right] \tag{21}$$

$$\left(\frac{\partial SV}{\partial a}\right)_{f'=f'_0} = -\frac{f'_0F_2}{2J_ucf}\left(\frac{1}{\rho J_uF_1}\right)^{1/2} \tag{22}$$

McCarthy et al.'s approach therefore provides an analytic expression for $(\partial SV/\partial a)$ in Eq. (2). Furthermore

$$\frac{J_1}{J_u} = \frac{1}{F_1^2}(F_1 + F_2) - \frac{F_2}{F_1^2\ln f'_0}\ln f' \tag{23}$$

which is shown as a straight line in the plots of J_1/J_u in the Supplementary Material, using $f'_0 = 10^9$.

The final issue concerns the effect of melt on these expressions. PM6 argued that the amount of melt present in the mantle was unlikely to exceed ~0.1%. If present, it was likely to form channels along the grain edges, because the dihedral angle is between 30° and 50°. They argued that such small amounts of melt in channels are unlikely to affect the bulk mechanical properties of the material. However, McCarthy and Takei (2011) have recently made a detailed study of the effect of melt on the elastic properties of borneol and found that the viscosity decreases by about two orders of magnitude at the solidus, even when the melt fraction is as small as 0.25%. Faul and Jackson (2007) have found the same behaviour in pure olivine. Though the physical process that produces this decrease is still unclear, the effect was included by decreasing the viscosity by 100 when the mantle solidus T_s was exceeded. The values of T_s that were used are listed in the notes to Table 1.

Table 1
Parameters to determine $V_s(P,T)$, Q_s^{-1} and η, estimated from Geophysics and Petrology.

	$\mu=\mu_0+(\partial\mu/\partial T)_P T+(\partial\mu/\partial P)_T P$			$\eta=\eta_0/a^\star$ (Eqs. (16)–(18))			Misfits	
	μ_0 at 0 K GPa	$(\partial\mu/\partial T)_P$ GPa/K units of 10^{-2}	$(\partial\mu/\partial P)_P$ –	$\log_{10}\eta_0$ $\log_{10}$(Pa s)	E kJ/mol	V_a m^3/mol units of 10^{-6}	M_1	M_2
PM_v1_2006	76.38	−1.168	2.19	20.44	409	10.		
PM_v2_2012	**72.66**	**−0.871**	**2.04**	**22.38**	**402.9**	**7.81**	**0.599**	**0.599**
PM_v2_2012, no atten. or η	72.73	−0.873	2.03	22.35	432.5	8.14	0.276	0.279
PM_v2_2012, no nodules	72.70	−0.873	2.02	22.54	479.5	7.16	3.33	3.37
PM_v2_2012, no ridge data	72.50	−0.872	2.06	22.24	384.2	8.15	0.452	0.454
PM_v2_2012 BK90	73.25	−0.896	1.93	22.91	292.8	3.93	0.669	0.731
S40RTS	74.94	−1.05	1.84	21.92	465.0	6.55	0.509	0.691
S362ANI_Vs	*74.12*	*-0.894*	*1.87*	*22.92*	*653.2*	*10.6*	*0.637*	*0.796*
S362ANI_Vsv	73.27	−0.891	1.94	21.73	440.6	10.8	0.655	0.703
SAW642ANb_Vs	*74.38*	*-0.902*	*1.76*	*23.51*	*441.3*	*9.23*	*0.740*	*0.793*
SAW642ANb_Vsv	72.32	−0.865	2.04	22.36	381.9	7.61	0.719	0.739
SEMum_Vs	*75.05*	*-0.938*	*1.81*	*22.91*	*585.2*	*9.71*	*0.642*	*0.820*
SEMum_Vsv	75.60	−0.948	1.74	22.36	516.3	10.0	0.640	0.777

Unrelaxed moduli (Laboratory)

	μ_0 at 0 K	$(\partial\mu/\partial T)_P$	$(\partial\mu/\partial P)_T$
Isaack (1992)	82	−1.36	1.8
Cammarano et al. (2003)	78.2	−1.3	1.5

Diffusion creep, dry olivine (Laboratory)

	$d\epsilon/dt=A\sigma^n d^{-p}\exp[-(E+PV_a)/RT]=\sigma/\eta$				
	$\log_{10}A$	n	p	E	V_a
Faul and Jackson (2007)	−15.92	1.37	3	484 ± 30	–
Hirth and Kohlstedt (2003)	−14.82	1	3	375 ± 50	2–10

Notes. The models used are PM_v2_2012 (this paper), S40RTS (Ritsema et al., 2011), S362ANI (Kustowski et al., 2008), SAW642ANb (Panning et al., 2010) and SEMum (Lekić and Romanowicz, 2011). The values listed for A assume that the stress is measured in pascals and the grain size (diameter) in metres. The values for η_0 use $P_r=1.5$ GPa and $T_r=1473$ K (Eqs. (15) and (16)), and are also in RMKS units. PM_v1_2006 is Priestley and McKenzie's (2006) model, PM_v2_2012 is model described in this paper. S40RTS is Ritsema et al. (2011) model for V_s. BK90 uses Brey and Kohler's (1990) expressions for temperature and pressure. NG85 uses Nickel and Green's (1985) expression for temperature, and T98 uses Taylor's (1998) expression for pressure. The weights applied to the misfits are $w_1=0.05$, $w_2=0.01$, $w_3=0.95$, $w_4=1.0$, $w_5=0.1$ (see Eqs. (26)–(30)) for all cases except PM_v2_2012 no atten. or η, which used $w_1=0.05$, $w_2=0.01$, $w_3=0.95$, $w_4=w_5=0.0$, PM_v2_2012 no nodules, which used $w_1=1.0$, $w_2=0.01$, $w_3=0.0$, $w_4=1.0$, $w_5=0.1$, and PM_v2_2012 no ridge data, which used $w_1=0.0$, $w_2=0.01$, $w_3=1.0$, $w_4=1.0$, $w_5=0.1$. Misfit M_1 is the value of the best fit, obtained with the parameter values listed, M_2 is that obtained using the values listed for PM_v2_2012. The preferred values of the parameters for PM_v2_2012 are shown in bold face, and those obtained from models using V_s, rather than SV alone, in italics. The values from Cammarano et al. (2003) are calculated from their Table A.1 using a value of X_{Fe} of 0.11 and modal proportions of olivine = 0.60, orthopyroxene = 0.21, clinopyroxene = 0.076 and garnet = 0.115. The values used for the solidus are 1300 °C (50 km), 1408 °C (75 km), 1510 °C (100 km), 1596 °C (125 km), 1661 °C (150 km), 1707 °C (175 km), 1742 °C (200 km).

3. Modelling and constraints

The new tomographic model for SV uses all the digital seismograms generated by the earthquakes listed in the centroid moment tensor (CMT) catalogue (Dziewonski et al., 1981) at distances $\leqslant 100°$. The number of such records is $\sim 3\times10^6$, or an order of magnitude more than were available in 2006. This increase allows us to use a lateral correlation length of 250 km rather than 400 km used by PM6 and a vertical one of 50 km. Only seismograms from the vertical components were used, principally because they have better signal-to-noise ratios than do the horizontal components. The shear wave velocities are therefore those of SV. As before, the inversion makes extensive use of higher mode dispersion, which principally controls the vertical resolution. The three dimensional model of SV is derived by first inverting individual surface waveforms in the 50–160 s period range for a path-average SV model using the automated version (Debayle, 1999) of the Cara and Lévêque (1987) technique. The path-average velocity models are then combined in a tomographic inversion to obtain the three dimensional SV wave speed model using the technique of Debayle and Sambridge (2004). The crustal model of Nataf and Ricard (1996) is used for the shallow structure. The method is described more fully by Priestley et al. (2012), and takes account of the dispersion produced by Q_s^{-1} (Debayle, 1999). We invert for the SV velocity and azimuthal anisotropy distribution as functions of depth, and refer to this new model as PM_v2_2012. Sieminski et al. (2004) have shown the resolution of tomographic models can be comparable to the wavelength of the surface waves if large numbers of well distributed paths are used. Whether the resolution can be improved by using finite frequency kernels instead of a correlation length is unclear. As Sieminski et al. show, the difference between the two approaches is reduced when the kernels for different frequency bands are combined. Moreover there can be important differences between the true finite frequency kernels for a laterally inhomogeneous velocity structure and those for a laterally homogeneous model.

The usefulness of velocity models obtained by inversion of surface wave velocities depends on their spatial and amplitude resolution, and on the presence of artefacts. Poor resolution is not as troublesome as are artefacts: spurious features that can seriously mislead any interpretation. Artefacts are often quite difficult to identify using the standard checkerboard tests. We prefer to test for them by generating synthetic seismograms from a model containing a feature of interest, followed by inversion. Priestley et al. (2012) tested PM_v2_2012 in this way by introducing a number of plates distributed over the Middle East, whose thickness 100 km and diameter 400 km (not 500 km as stated in error in the caption to their Fig. 4), and whose SV velocity was 10% greater than the reference velocity. They generated synthetic seismograms from this velocity model which they then inverted. The horizontal and vertical extent of the plates was well resolved with, importantly, only minor artefacts. The amplitude of the SV anomaly was well reproduced when the plates extended from 50 to 150 km, but was only about 5% greater than the reference velocity when the depth extent was from 150 to 250 km.

The upper part of the mantle consists of peridotite, and therefore contains minerals with anisotropic elastic moduli. The orientation of the symmetry axes of these minerals is controlled by their deformation history. Though seismic information can provide some constraints, it cannot be used to determine the 21 relevant parameters. Since we are principally interested in using seismic information to estimate mantle temperature, this difficulty can be avoided if the seismic information could be used to define a scalar function of the elastic parameters that is invariant under rotation about any axis. Unfortunately it is not clear how even this limited problem can be solved.

Smith and Dahlen (1973) showed that the general expression for Rayleigh and Love wave propagation velocity V in an anisotropic solid in the direction with azimuth ϕ is

$$V = A + B\cos 2(\phi+\phi_1) + C\cos 4(\phi+\phi_2) \tag{24}$$

where A, B, C, ϕ_1 and ϕ_2 are constants, and $B \gg C$ for Rayleigh waves. In the discussion below, values of the constants for Rayleigh waves are denoted with a subscript R. PM_v2_2012 uses this expression with $C_R = 0$. If ϕ is measured from a vertical mirror plane of symmetry $\phi_1 = \phi_2 = 0$. In contrast PREM, S362ANI, SAW642ANb and SEMum are transversely isotropic models, which are unchanged by rotation through any angle about the vertical z axis, denoted by ∞_z, and by a reflection m_z in a plane normal to this axis. Such symmetry is not easily produced by any of the simple types of deformation. For instance pure shear resulting from horizontal plate motion in the x direction generates a velocity gradient tensor, and hence a deformation gradient tensor (Malvern, 1969), with monoclinic symmetry $2_y/m_y$, where 2_y is a horizontal diad axis along the y axis and m_y is a mirror plane normal to this axis (Tommasi, 1998). Such symmetry gives rise to thirteen independent elastic moduli (Nye, 1957). Pure shear shortening in the x direction produces a velocity gradient tensor with orthorhombic symmetry mmm with nine elastic moduli. The velocity gradient tensor only has transversely isotropic symmetry when uniaxial extension or shortening occurs in the z direction. The only part of the deforming mantle likely to have such symmetry is on the axis of rising or sinking plumes.

Transversely isotropic models are often tabulated in terms of the Voigt average V_s and an anisotropic parameter ξ, defined by

$$V_s^2 = \frac{2SH^2 + SV^2}{3} = \frac{(2\xi+1)}{3}SV^2, \quad \xi = SH^2/SV^2 \tag{25}$$

where SV is the velocity obtained from Rayleigh waves and SH from that of Love waves. V_s is invariant with respect to rotations about a vertical, but not a horizontal, rotational axis. The same is true for SV obtained from A_R. However, unlike Eq. (25), Eq. (24) is valid for any mildly anisotropic material (Smith and Dahlen, 1973). Furthermore the value of V_s is dominated by that of SH from Love waves. Love wave dispersion is less than that of Rayleigh waves, and, because horizontal seismograms are noisier than vertical ones, is less well determined. For these reasons we prefer to use A_R to determine the parameters that relate shear velocity and temperature.

The parameters obtained from A_R for PM_v2_2012 and S40RTS (Ritsema et al., 2011), and from both A_R and V_s for three other recently published tomographic models largely based on surface waves: S362ANI (Kustowski et al., 2008), SAW642ANb (Panning et al., 2010) and SEMum (Lekić and Romanowicz, 2011), are listed in Table 1. For the transversely isotropic models SV was calculated from V_s using Eq. (25). Both S40RTS and SAW642ANb use PREM as a reference model. Both therefore have a discontinuity at 220 km, which leads to a corresponding temperature discontinuity at this depth. To avoid this problem only velocities above 220 km from these two models were used, both for the parameterisation and

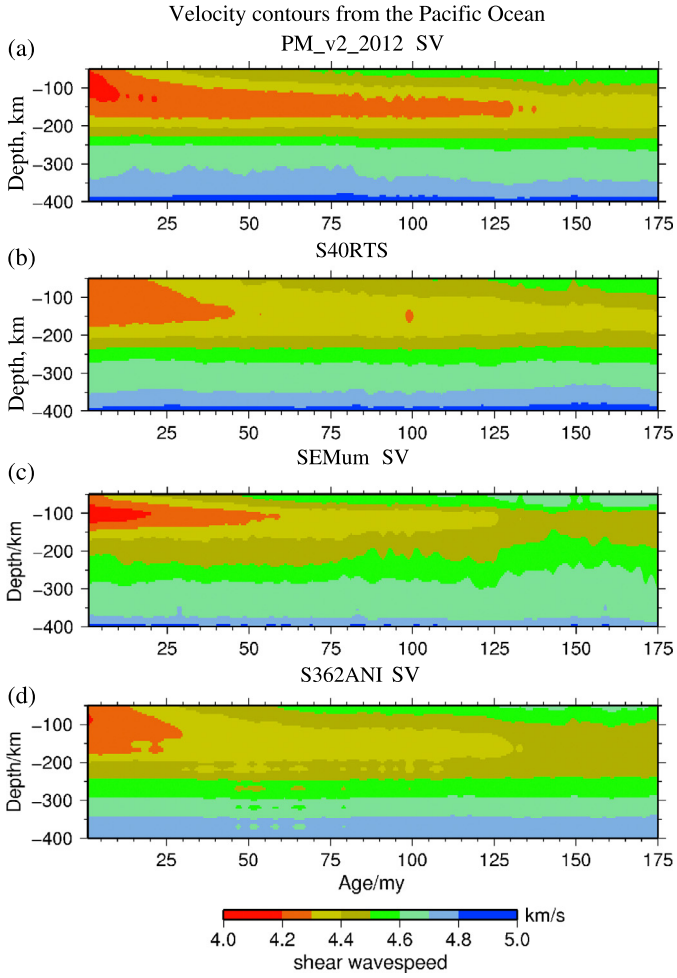

Fig. 2. Profiles of SV from tomographic models of the Pacific, stacked as functions of age at intervals of 2 Ma, using ages from Müller et al. (2008) and excluding the regions that Crosby et al. (2006) classified as not having typical oceanic structure. (a) PM_v2_2012, (b) Ritsema et al. (2011), (c) Lekić and Romanowicz (2011), (d) Kustowski et al. (2008).

to estimate the lithospheric thickness. Fig. 2 shows stacks of four models of SV for the Pacific, excluding those regions that Crosby et al. (2006, their Fig. 2) classified as having atypical crustal structure. Figs. 3c and 3d show that excluding such regions and using an order of magnitude more seismograms reduce the standard deviation of SV as a function of depth and age by almost an order of magnitude. PM_v2_2012, SEMum and S362ANI show an increase in velocity with plate age at depths of less than 175 km, and at a slightly greater depth in S40RTS, whereas the plate thickness that best fits the variation of depth with age in the Pacific is about 90 km (Crosby et al., 2006). This difference partly results from the limited vertical resolution of the models, which in the case of PM_v2_2012 is no better than 50 km, and partly from the thermal boundary layer shown in Fig. 1a. However, the thermal structure within the mechanical boundary layer is controlled by conduction alone, and the temperatures at depths of 50 and 75 km from the plate model should not be affected by convection within the thermal boundary layer.

We used the same thermal model of the oceanic lithosphere as PM6 to estimate $SV(T, z)$ at depths of 50 and 75 km. PM6 used pressure and temperature estimates from garnet peridotites brought to the surface by magmas. The use of such estimates is only valid if the thermal structure of the lithosphere has remained unchanged since the nodules were extracted. The velocity models were linearly interpolated in three dimensions to provide an es-

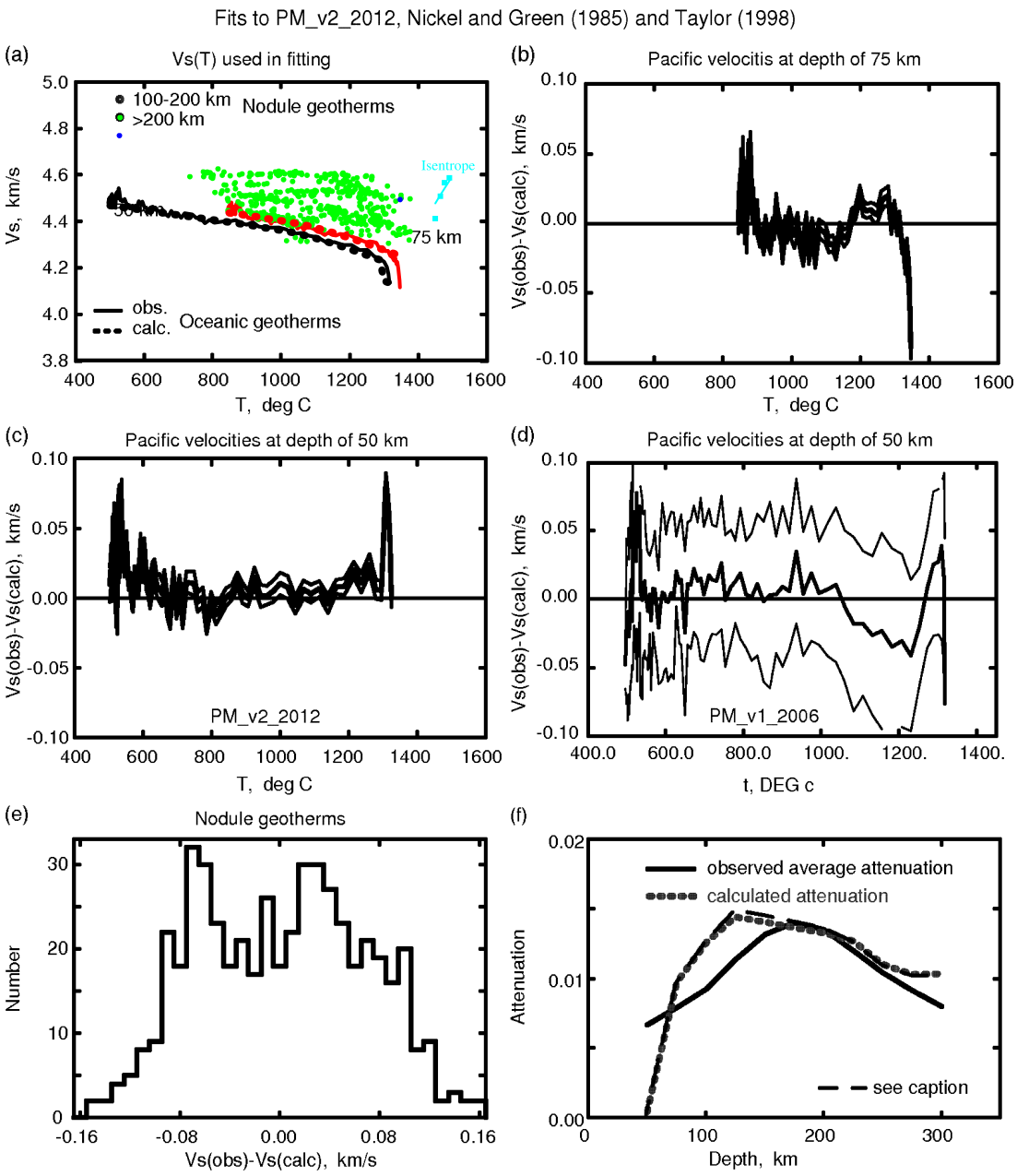

Fig. 3. Fits to PM_v2_2012 and pressure and temperature estimates from a thermal model of the oceanic lithosphere and from nodules estimated from their mineralogy using Nickel and Green's (1985) barometer and Taylor's (1998) thermometer. The values of the parameters are given in bold face in Table 1. (a) shows the velocity data used in the fit (see Section 3). The solid black line shows the velocities from Fig. 1a at a depth of 50 km, the red line those at 75 km. The green dots show the interpolated velocities at the locations and depths of the nodules, and the pale blue dots labelled 'Isentrope' are horizontal averages of the velocity beneath the Pacific at depths of 225–300 km at 25 km intervals. The dashed red and black lines and the continuous pale blue line show values of SV calculated from the parameterisation. (b) and (c) show the difference between the observed and calculated velocities at depths of 75 and 50 km respectively, with mean misfits of 0.006 and 0.018 km/s and standard deviations of 0.033 and 0.020 km/s. The middle curves show the stacked values from Fig. 2a, and the upper and lower curves one standard deviation of the values used to obtain the stack. (d) as for (c) but using PM_v1_2006 from PM6. (e) is a histogram showing the difference between the observed and calculated velocities for the nodules. The ordinate shows the number of values in each 0.01 km/s interval. 4 values are outside the plotted range. The mean misfit is 0.017 km/s and the standard deviation is 0.068 km/s. (f) Comparison of the observed and calculated attenuation, Q_s^{-1}, beneath the Pacific. The rms difference between the observed value, Ref. [2] from Dalton et al. (2009), and that calculated from the parameterisation between depths of 150 and 300 km is 0.0020. The misfit of $\log_{10}$(viscosity), H_5, over the same depth range is 1.16. The thin dashed line shows the attenuation calculated from the parameters determined from the velocities alone (see Table 1), not using either the attenuation or viscosity. The rms misfit between the observed and calculated attenuation is 0.0021, and the value of H_5 is 1.04. (For interpretation of the references to color in this figure legend, the reader is referred to the web version of this article.)

timate of SV at the location and depth from which each nodule was extracted. Data from 38 pipes were used, of which 24 are in South Africa, taken from Nimis and Grütter (2010) and Janney et al. (2010), consisting of 511 analyses of the mineral compositions in individual nodules. Nimis and Grütter (2010) discuss a number of different expressions that have been used to estimate P and T from the nodule mineralogy, and recommend the use of Taylor's (1998) two pyroxene thermometer and Nickel and Green's (1985) barometer. They argue that this combination gives better agreement with the laboratory experiments than does the more widely used combination of Brey and Kohler's (1990) thermometer and barometer. Both are used below, to discover how much effect different approaches to estimating P and T have on the values of the seismological parameters. Tables 1 and 2 show that there is

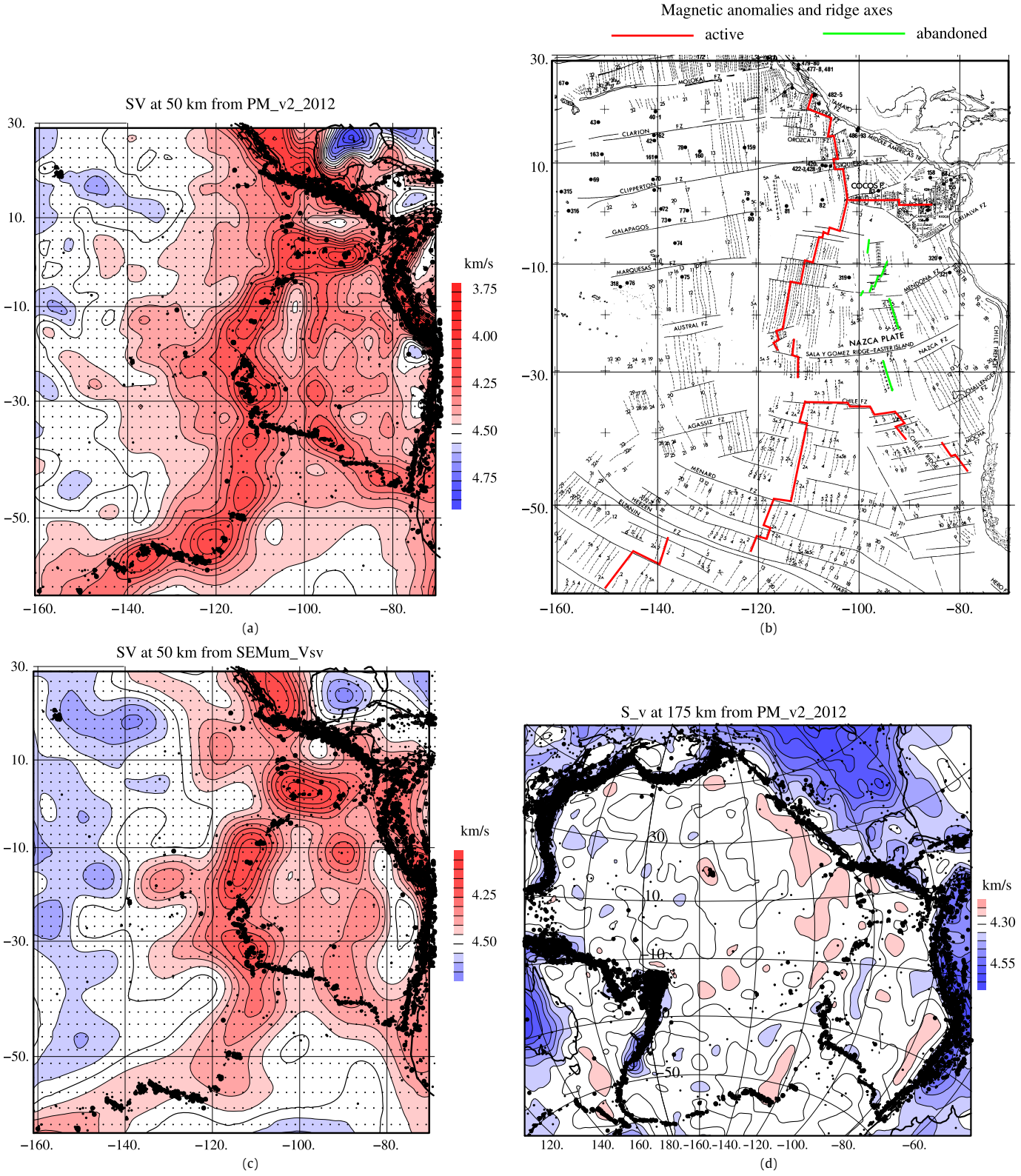

Fig. 4. (a) SV at a depth of 50 km from PM_v2_2012. In this and later figures the smallest black dots are the locations at which the velocity is given in the model, the larger dots are earthquake epicentres between 1960 and 2007 with magnitudes greater than about 4. The largest dots are epicentres of earthquakes whose magnitude M $\geqslant$ 6.5 between 1900 and 1963, and those with M $\geqslant$ 5.5 after 1964 (Engdahl et al., 1998 and updates). (b) Magnetic anomalies from Owen (1983), showing the location of the active (red) and abandoned (green) spreading centres (Okal and Bergeal, 1983; Goff and Cochran, 1996; Lonsdale, 2005). (c) As for (a) but using the velocity model SEMum_Vsv. (d) As for (a) but at a depth of 175 km. (For interpretation of the references to color in this figure legend, the reader is referred to the web version of this article.)

excellent agreement between the two petrological parameterisations.

Three further constraints were applied that were not used in PM6. The first depends on the average value of the mantle potential temperature. Decompression melting that occurs beneath spreading ridges can only generate constant thickness oceanic crust (White et al., 1992) if the potential temperature of the mantle is constant. The resulting crustal thickness depends on both the

Table 2
Lithospheric thicknesses.

Mean differences in km, left-top

	br_mineral	ng_mineral	br_maxwell	ng_maxwell	SEMum_Vsv
br_mineral	0.0	5.5	19.6	17.8	−27.6
ng_mineral	−5.5	0.0	14.1	**12.3**	−33.1
br_maxwell	−19.6	−14.1	0.0	−1.8	−47.2
ng_maxwell	−17.8	**−12.3**	1.8	0.0	−45.4
SEMum_Vsv	27.6	33.1	47.2	45.4	0.0

Mean s.d. in km, $\sqrt{\sum(\text{left-top-mean diff.})^2/N}$

	br_mineral	ng_mineral	br_maxwell	ng_maxwell	SEMum_Vsv
br_mineral	0.0	7.7	26.1	26.5	37.8
ng_mineral	7.7	0.0	23.3	**23.7**	37.6
br_maxwell	26.1	23.3	0.0	1.5	29.0
ng_maxwell	26.5	**23.7**	1.5	0.0	28.9
SEMum_Vsv	37.8	37.6	29.0	28.9	0.0

Notes. br_ uses Brey and Kohler's (1990) expressions for temperature and pressure. ng_ uses Nickel and Green's (1985) expression for temperature and Taylor's (1998) for pressure. _mineral are thicknesses determined from estimates of P and T from the mineralogy alone. _maxwell are thicknesses determined from an S_v model using the appropriate parameters to estimate T. The lithospheric thicknesses and locations of the 38 pipes used are listed in the supplementary material. The numbers in bold face are those of the preferred model used to produce Figs. 5b, 6, 7, and the lithospheric thicknesses in the Supplementary Material.

potential temperature and the entropy of melting ΔS. Kojitani and Akaogi (1997) obtained a value of 400 $JK^{-1}kg^{-1}$ for ΔS, when a potential temperature of 1315 °C is required to generate an oceanic crustal thickness of 7 km. The isentropic temperature gradient $(\partial T/\partial z)_s \simeq 0.6\,°C/km$ can then be used to calculate the average actual temperature within the convecting interior of the upper part of the mantle at depths between 225 and 300 km. These depths are greater than those from which nodules are brought to the surface. The corresponding values of SV were calculated by averaging the values beneath the Pacific. Fig. 2 shows that the values at these depths are independent of lithospheric age and are therefore not affected by plate cooling.

The last two constraints make use of McCarthy et al. (2011) approach, and involve estimates of attenuation and viscosity. Dalton et al. (2009) generated two attenuation models for the vertical variation in Q_s^{-1} beneath sea floor older than 100 Ma. The values at depths of 150–300 km from their model (Ref. [2]) were used as a constraint. The final constraint that was used was the average of $\log_{10}$(viscosity) over the depth range 150–300 km. Zhao et al. (2012) determined a value of 4.2×10^{20} Pa s for the average global viscosity between depths of 100 and 670 km.

4. Fits

The parameters were calculated by minimising H where

$$H=\sum_{i=1}^{N} w_i H_i \tag{26}$$

H_1 was calculated from the stacked oceanic velocities V_i(obs) and their standard deviations σ_i:

$$H_1=\left[\frac{1}{N}\sum_{i=1}^{N}\left(\frac{V_i(\text{obs})-V_i(\text{calc})}{\sigma_i}\right)^2\right]^{1/2} \tag{27}$$

The same expression was used for H_2, the average velocities at depths of 225 to 300 km beneath the Pacific. The misfit of the nodule velocities, H_3, was obtained from

$$H_3=\left[\frac{1}{N}\sum_{i=1}^{N}\left(V_i(\text{obs})-V_i(\text{calc})\right)^2\right]^{1/2} \tag{28}$$

that of the attenuation Q_i^{-1}(obs) using

$$H_4=\left[\frac{1}{N}\sum_{i=1}^{N}\left(Q_i^{-1}(\text{obs})-Q_i^{-1}(\text{calc})\right)^2\right]^{1/2}/Q_{\text{mean}}^{-1} \tag{29}$$

where Q_{mean}^{-1} is the average observed attenuation, and that of the viscosity

$$H_5=\left[\frac{1}{N}\sum_{i=1}^{N}\left(\log_{10}\left(\eta(\text{ref})\right)-\log_{10}\left(\eta_i(\text{calc})\right)\right)^2\right]^{1/2} \tag{30}$$

The best fitting parameters for each of the models and the weights w_i used for each fit are given in Table 1.

Probably the most important result is that it is possible to match all the constraints obtained from PM_v2_2012 quite well using a single the value each of the six parameters, listed in bold face in Table 1. The fits are shown in Fig. 3. The same is true for the other four models (see Table 1, and Supplementary Material). The rms misfits to the SV velocities from spreading ridges are $\sim4\times10^{-2}$ km/s, and the velocity estimates from tomography are unlikely to be more accurate. The agreement between the calculated values for the nodules and those from the SV models is slightly less good. This difference may result from the limited horizontal resolution of the shear wave velocity models. The misfits for the V_s models are similar to those for SV. As expected, misfit M_2, calculated using the parameters that best fit PM_v2_2012, is slightly greater than misfit M_1, obtained when all six parameters are allowed to vary. If the parameters for SEMum_Vsv are excluded (see below), the activation energies obtained from SV models range from 380 to 465 kJ/mol. The fit to PM_v2_2012 was also carried out without using the attenuation and viscosity constraints, without the ridge data, and without the nodule data (see Table 1). In all three cases misfit M_1 is almost the same as M_2. Therefore the estimates of temperature from nodule petrology are consistent with those from cooling plate models. Furthermore the agreement between the observed attenuation and that calculated from the parameters fitted to the velocities alone, shown in Fig. 3f, suggests that McCarthy et al.'s expressions may be valid in the seismically important range $10^8 \leqslant f' \leqslant 10^{11}$. Another important result is that different values of the parameters are required to match the different tomographic models. Therefore the function $T(SV,z)$ depends on the tomographic method used to obtain SV, and cannot be obtained from laboratory experiments alone.

The agreement between the calculated and observed values of the attenuation and viscosity is less good than is that for SV, but

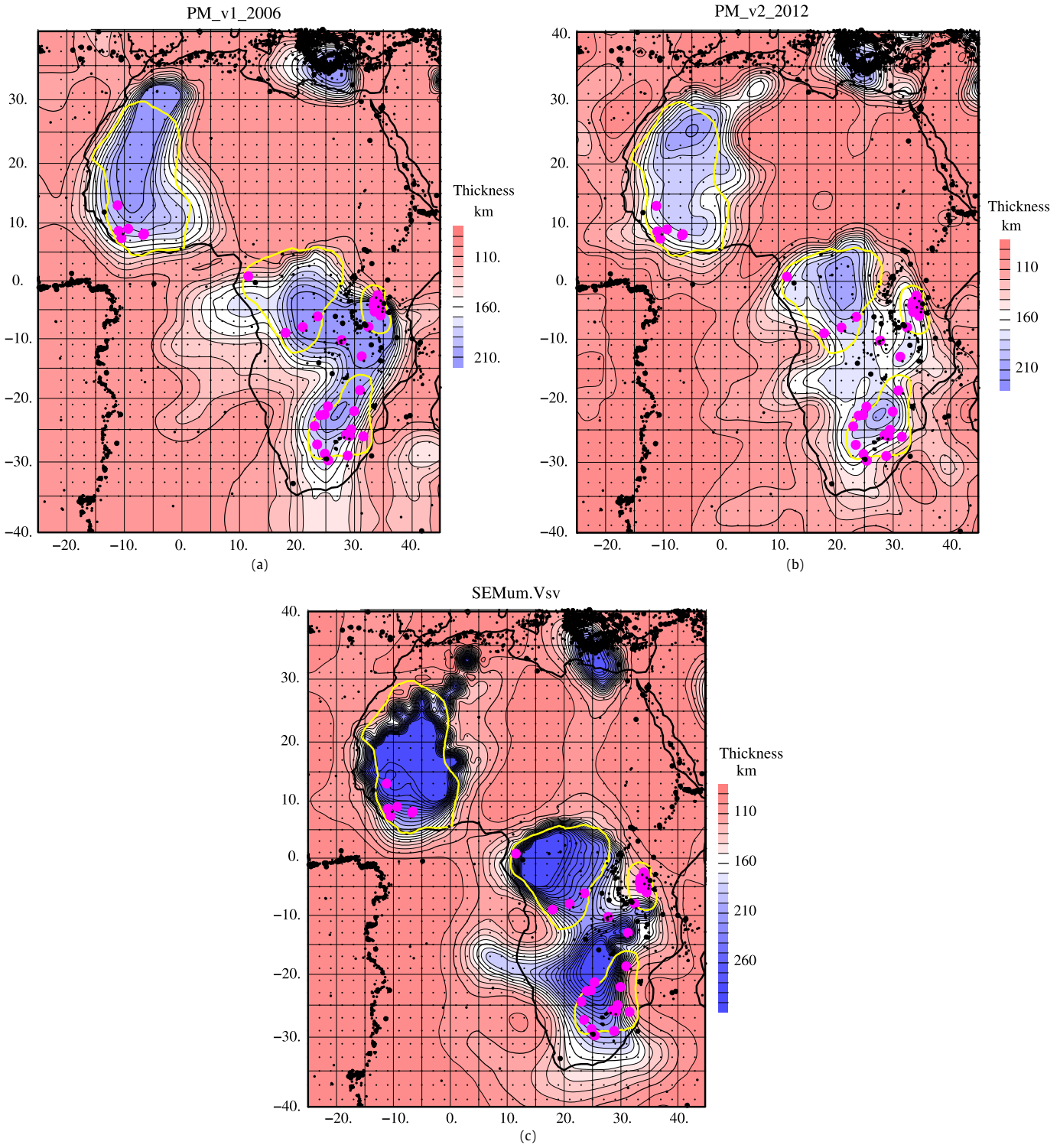

Fig. 5. (a) Thickness of the African lithosphere from PM6. The magenta dots mark the locations of diamond-bearing kimberlites, and the yellow lines the surface outcrops of cratons (see the caption to Fig. 4a for the definitions of the black dots). (b) as for (a), but calculated from PM_v2_2012. (c) as for (a), but calculated from SEMum_Vsv. (For interpretation of the references to color in this figure legend, the reader is referred to the web version of this article.)

the attenuation is difficult to determine from the seismic data, and there is poor correlation between the various models that have been published (see Dalton et al., 2009). The viscosity of the mantle is even more difficult to estimate. Zhao et al. (2012) were able to model the vertical and horizontal GPS velocities in Fennoscandia to their satisfaction with a constant viscosity between depths of 100 and 670 km. Estimates of mantle viscosity from shear wave velocity models discussed in the next section vary strongly, both vertically and horizontally.

The temperatures used to estimate the lithospheric thickness are obtained by inverting the expressions in Section 2. Because $SV(T)$ is a strongly nonlinear function of T, the accuracy of the temperature estimates increases with increasing temperature. If the standard error in SV is that determined from the misfit to

the nodule data, 0.069 km/s, at a depth of 50 km the corresponding temperature error is about 360 °C at temperatures below 900 °C, but decreases to 110 °C close to the melting temperature of 1300 °C. Principally for this reason, estimated temperatures lower than 900 °C were not used when determining the lithospheric thicknesses (see Figs. 1b and 1c).

Table 1 compares the values of the parameters obtained from the fitting process with those from laboratory experiments. The general agreement is good. The values of $\mu(0,0)$ from such experiments are slightly greater than those from the fits, as are those of $|(\partial\mu/\partial T)_P|$, whereas the laboratory values of $(\partial\mu/\partial P)_T$ are slightly smaller. The activation energies are well constrained by the fitting process, but the constraints on activation volumes are poorer: there is a trade-off between $(\partial\mu/\partial P)_T$ and V_a. The values of E and V_a from the fits agree well with those tabulated by Hirth and Kohlstedt (2003) and by Faul and Jackson (2007). If the values of E and V_a determined from the geophysical data are taken to be the same as those of creep experiments, then Hirth and Kohlstedt's expression for the creep rate in Table 1 can be combined with Eqs. (8), (15)–(17) to give an expression for the grain size (diameter) d

$$d^3 = A\eta_0 \exp\left[-(E + P_r V_a)/RT_r\right] \tag{31}$$

where the values of A and η_0 are given in Table 1, $P_r = 1.5$ GPa and $T_r = 1473$ K. Substitution gives a grain diameter of about 4 mm, which is within the range found in mantle nodules. The value of η_0 in Table 1 depends on global information from the mantle at depths of less than 300 km. Therefore this estimate of the grain size is also a global estimate from the same shell.

It is not obvious how to reconcile Hirth and Kohlstedt's values of E and V_a with those from laboratory diffusion data. They showed that the creep rate is proportional to d^{-3}, where d is the grain diameter, which is the expected behaviour for grain boundary, or Coble, creep (see Karato, 2008, p. 132). But Farver and Yund (2000) obtained an activation energy of 203 kJ/mol for Si grain boundary diffusion. Si is the slowest diffusing species, and so its movement should be rate limiting. It is therefore surprising that the difference between the activation energies for grain boundary creep and diffusion are so large. What is even more surprising is that the activation energy for body diffusion of Si, measured by Fei et al. (2012) to be 410 ± 30 kJ/mol, agrees with both that obtained here by fitting the geophysical and petrologic information and that of Hirth and Kohlstedt (2003).

5. Lithospheric thickness, attenuation and viscosity

The parameters obtained in the last section can now be used to obtain estimates of the lithospheric thickness, S-wave attenuation and viscosity. Since the processes that control the temperature in the lithosphere beneath continents are not yet well understood, it is not obvious how lateral velocity variations in such regions can be distinguished from artefacts generated by the inversion process. However, at depths of less than about 100 km within normal oceanic lithosphere (Crosby et al., 2006) the temperature variation with depth is well constrained and is a function only of the lithospheric age. Therefore the shear wave velocity profile should also be a function of age alone. This argument was used in Section 3 to help determine the parameters. It also provides a convenient method of assessing both the true resolution of models of SV and of examining them for artefacts. A particularly useful area for this purpose is the SE Pacific, shown in Fig. 4. Fig. 4a shows a map of SV for this region at a depth of 50 km, together with the earthquake locations from Engdahl et al. (1998 and updates). The map is dominated by the low velocity belt associated with the East Pacific and the Galapagos spreading ridges. Many of the earthquakes associated with these ridges are on transform faults. But there is also a belt of low velocity on the Nazca Plate extending from about 0°N, −95°E to −37°N, −95°E which is not seismically active. This belt marks the location of an abandoned ridge (Okal and Bergeal, 1983; Goff and Cochran, 1996; Lonsdale, 2005) which is clearly visible in the magnetic anomaly patterns (Fig. 4b). The nominal horizontal resolution of the model is 250 km, and the clear resolution of the failed ridge in this region shows that the actual horizontal resolution is similar to the nominal resolution. Furthermore, this part of the Pacific is one of the least well resolved regions of the tomographic model PM_v2_2012. The horizontal resolution beneath the continents is therefore also likely to be close to the nominal resolution. This conclusion is in agreement with the resolution tests carried out by Priestley et al. (2012). Of the four other models of SV (see Supplementary Material), only SEMum (Fig. 4c) has a low velocity feature in this region. Whether this feature is related to the abandoned ridge is unclear, because it lies between 500 and 800 km further east.

The shear wave velocity models for the Pacific also provide information about their vertical resolution, because ridges are not expected to be associated with thermal upwelling in the mantle below the plates. Figs. 2a and 4d show that the low velocities beneath the spreading ridges are confined to the region above 175 km (see also Supplementary Material). The thickness of old plates, including the thermal boundary layer, is probably about 150 km (see Introduction). Therefore the absence of a correlation between age and velocity in Fig. 4d suggests that the vertical resolution is ∼50 km. Fig. 4d also shows a low velocity region beneath Hawaii, where the rising plume spreads out beneath the lithosphere. As expected, no such feature is visible in Fig. 4a, because the lithosphere beneath the islands is not rifted. The expressions in the previous section allow the temperature to be calculated from the shear velocity. Because the vertical resolution is ∼50 km, velocities at depths of less than 90 km may be reduced by vertical smearing between the crust and the mantle. The approach therefore cannot determine continental lithospheric thicknesses of less than ∼100 km.

A quantitative comparison between lithospheric thicknesses from SV models and that from nodule mineralogy is shown in Table 2 for the 38 pipes used for the parameterisation. The rms misfit of the temperatures to the geotherms is about 60 °C in all cases. The difference between the thicknesses obtained using Brey and Kohler's (1990) barometer and thermometer and that of Nickel and Green (1985) and Taylor (1998) is small, though the agreement between the thicknesses from the nodules and the shear wave velocities is slightly better for the latter, which was therefore used to calculate the lithospheric thickness. The average thickness of the lithosphere estimated from PM_v2_2012 is 14 km less than that estimated from the nodules. The standard deviation, of 23 km, is larger, perhaps because of short wavelength variations in lithospheric thickness which are not resolved by the surface waves. Table 2 shows that the lithospheric thickness determined from PM_v2_2012 is likely to be accurate to 20–30 km. Table 2 also shows that the lithospheric thicknesses from SEMum are greater than the petrological estimates. This difference results from the velocities beneath cratons being higher in SEMum than they are in any of the other models of SV (Lekić and Romanowicz, 2011).

Fig. 5 shows three maps of the lithospheric thickness beneath Africa. Fig. 5a uses the velocity model PM_v1_2006 and parameter values from PM6, whereas Fig. 5b uses PM_v2_2012 and the parameters determined from Nickel and Green's (1985) geothermometer and Taylor's (1998) geobarometer. The two maps are similar, and in both thick lithosphere underlies the cratons. But the resolution is considerably better in Fig. 5b. In particular there is thin lithosphere beneath the Western Rift, at 0°N, 29°E, the Bie Dome in Angola, at −12°N, 15°E and the Windhoek Dome at −23°N, 17°E, all of which are believed to be convectively sup-

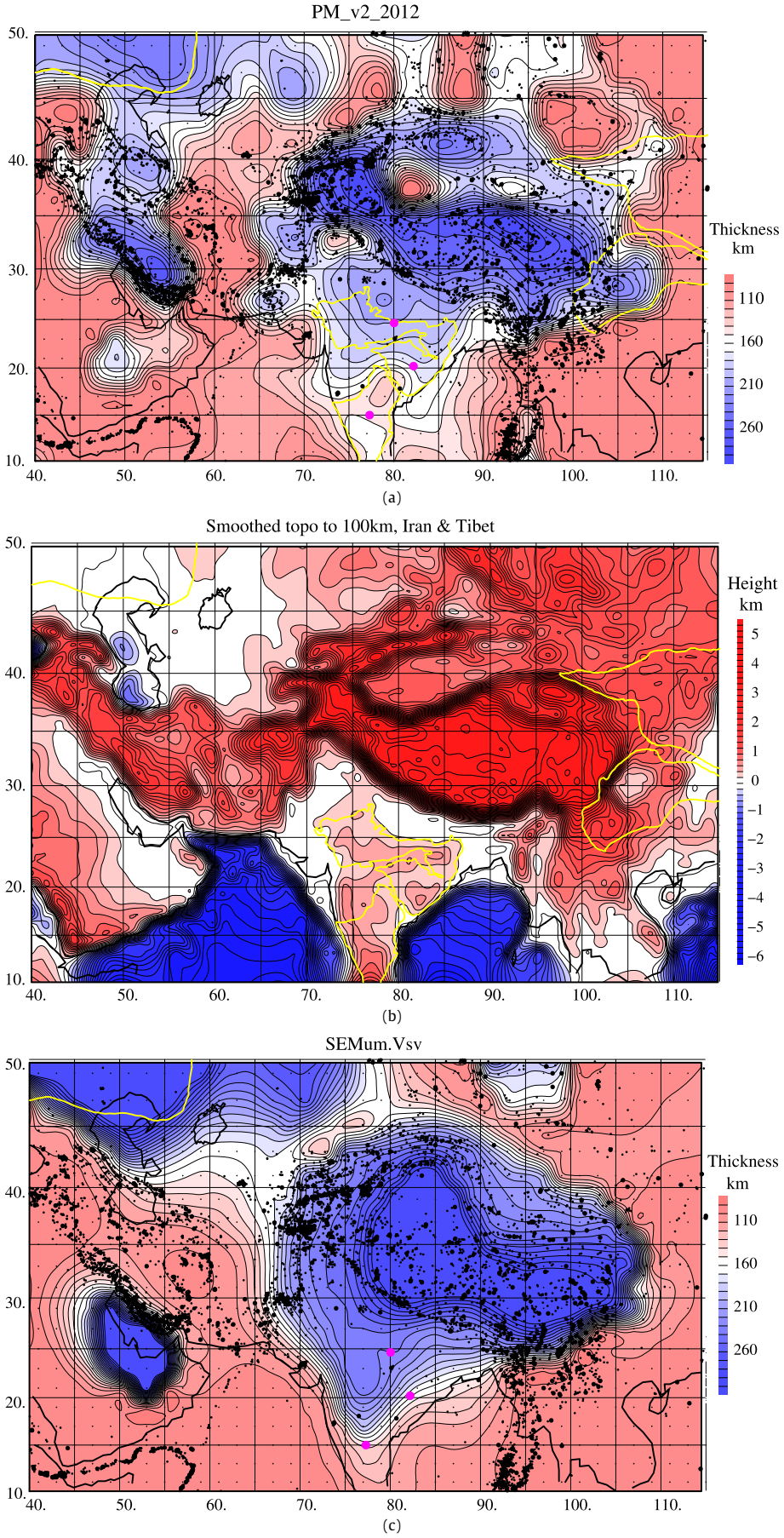

Fig. 6. (a) As for Fig. 5a, calculated from PM_v2_2012. (b) Topography smoothed with a box car filter of 100 km × 100 km. (c) As for Fig. 5c, calculated from SEMum_Vsv.

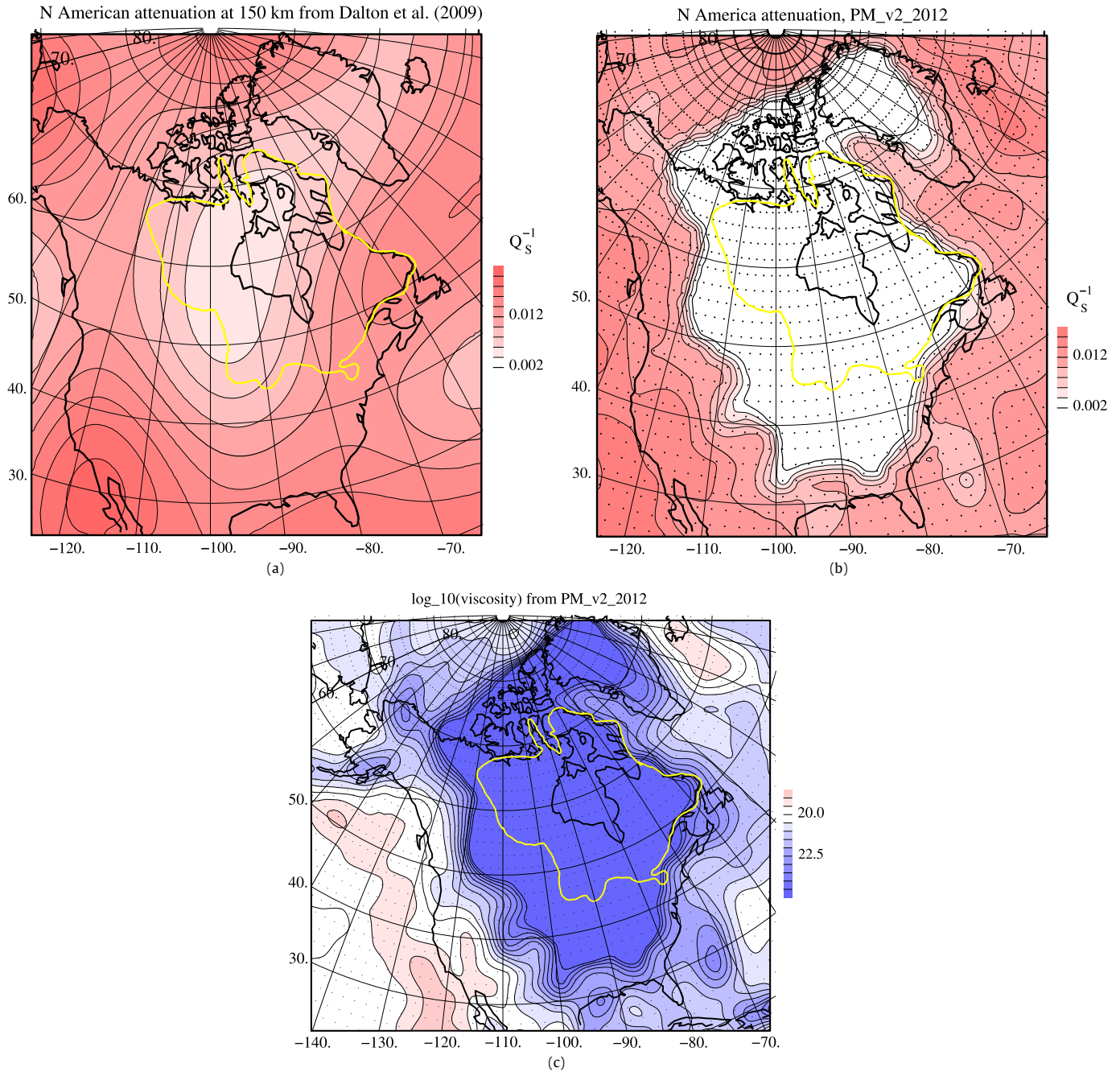

Fig. 7. (a) Q_s^{-1} attenuation for North America at a depth of 150 km from Dalton et al. (2009). (b) As for (a) but from PM_v2_2012. (c) $\log_{10}\eta$, where η is the viscosity in Pa s, at a depth of 150 km from PM_v2_2012.

ported (McKenzie, 2010). Lithospheric thicknesses from SEMum (Fig. 5c) show a similar distribution to those from PM_v2_2012, but are everywhere thicker beneath the cratons. The sudden increase in thickness at the craton boundaries is likely to be an artefact. Both Figs. 5a and 5c show an area of thick lithosphere off the west coast of southern Africa, at about −5°N, 10°E in Fig. 5a and −17°N, 7°E in Fig. 5c. Since the thickness of the oceanic lithosphere is expected to be a function of age alone, the question arises as to whether these features are artefacts. In the case of Fig. 5a, Priestley et al. (2008) showed that this is indeed the case, and their argument is supported by the absence of this feature in Fig. 5b.

Maps of the lithospheric thickness from PM_v2_2012 for continental regions are in general similar to those from PM_v1_2006, though the resolution of the boundaries of the cores is improved. Only the thick lithosphere beneath Tibet and Iran was resolved in PM6. Comparison of Figs. 6a and 6b shows that all the main mountain ranges of central Asia now undergoing shortening are underlain by thick lithosphere. This correspondence is less obvious in Fig. 6c, generated from SEMum and in the maps from other models shown in the Supplementary Material. Priestley et al. (2012) showed that the thick lithosphere beneath the Zagros, in the region of 32°N, 53°E, was a real resolved feature using synthetic seismograms. The feature near 25°N, 53°E in Fig. 6c may be generated by the same structure. If this is indeed the case, then, like the anomaly in Fig. 4c, it has been displaced. McKenzie and Priestley (2008) proposed that these regions of thick cold lithosphere were convectively stable because they consist of harzburgite, formed by melt extraction; the density reduction resulting from such depletion is about 60 kg m^{-3}.

An important advantage of McCarthy et al. (2011) approach is that it generates estimates of the shear wave attenuation and viscosity from the shear wave velocity model. However, it is not yet clear whether McCarthy et al.'s expressions are valid in the seismically important range where the anelastic effects are small, where at present there is no laboratory control. Fig. 7a shows a map of Dalton et al. (2009) estimates of attenuation for North America at a depth of 150 km, obtained from modelling the seismic amplitudes. Fig. 7b shows that obtained at the same depth from PM_v2_2012 using the expressions in Section 2, and shows much greater detail. Like the values in Table 1, the general agreement between Figs. 7a and 7b suggests that McCarthy et al.'s expressions may also apply in the seismically important range.

The anharmonic contribution to the shear modulus is related to the reciprocal of the viscosity (see Eq. (11)). At temperatures below ~1100 °C this contribution becomes small and is poorly resolved. The viscosity at 1100 °C is about 10^{23} Pa s. Viscosities calculated from SV in excess of this value are therefore unlikely to be accurate. Fig. 7c shows a map of $\log_{10}$(viscosity) at a depth of 150 km, obtained from Eq. (7) and the parameters in Table 1. At this depth the calculated viscosity varies by at least two orders of magnitude between the oceanic asthenosphere and the North American core. It seems likely that such variability will affect the isostatic response to glacial loading.

6. Discussion and conclusions

The velocity model PM_v2_2012 described here is given in the Supplementary Material. It is based on about an order of magnitude more seismograms than were used to generate the model described in PM6. As expected from the arguments of Sieminski et al. (2004), such dense coverage produces a lateral resolution of ~250 km, similar to that of both the wavelength of the surface waves and the correlation length. It is combined with a variety of geophysical and laboratory estimates of mantle temperature, obtained from models of spreading ridges, from pressure and temperature estimates from garnet peridotite nodules, from the average potential temperature of the convecting mantle, from the radial variation in attenuation Q_s^{-1}, and from average mantle viscosity, to obtain expressions for $SV(P,T)$, $Q_s^{-1}(P,T)$ and $\eta(P,T)$. The approach is described by McCarthy et al. (2011) and uses the viscosity to calculate the Maxwell relaxation time, which is then used to obtain a dimensionless frequency. The values of the parameters involved depend on the velocity model and on the geothermobarometer used in the parameterisation. The values of five of these parameters agree with estimates from laboratory experiments. The sixth depends on the grain size, and the expression for this parameter determined from laboratory experiments gives a mantle grain diameter of ~ 4 mm. Another advantage of McCarthy et al. (2011) approach is that it provides estimates of Q_s^{-1} and η. Comparison with the limited independent estimates of these two parameters suggests that the values obtained from McCarthy et al.'s approach are in general agreement with the geophysical observations.

An important use of the temperature obtained from SV is to estimate the lithospheric thickness, using geothermal models of the lithosphere. Estimates from the new model agree with those from PM6, though the horizontal resolution is better: ~250 km instead of ~400 km. This improvement shows that thin lithosphere in eastern and southern Africa correlates with the location of the East African Rift and with the plumes beneath Angola and Namibia. In Asia thick lithosphere is associated with active continental shortening. The improved resolution of the new model is likely to allow variations in lithospheric thickness to be correlated with other geological features.

Acknowledgements

We are grateful to R. Cooper, C. Dalton, D. Kohlstedt, H. Grütter, C. McCarthy, P. Shearer, Y. Takei and three anonymous referees for their help.

Appendix A. Supplementary material

Supplementary material related to this article can be found online at http://dx.doi.org/10.1016/j.epsl.2013.08.022.

References

Brey, G.P., Kohler, T., 1990. Geothermobarometry in four-phase lherzolites: II. New thermobarometers and practical assessment of existing thermobarometers. J. Petrol. 31, 1353–1378.
Cammarano, F., Goes, S., Vacher, P., Giardini, D., 2003. Inferring upper-mantle temperatures from seismic velocities. Phys. Earth Planet. Inter. 138, 197–222.
Cara, M., Lévêque, J., 1987. Waveform inversion using secondary observables. Geophys. Res. Lett. 14, 1046–1049.
Crosby, A.G., McKenzie, D., Sclater, J.G., 2006. The relationship between depth, age and gravity in the oceans. Geophys. J. Int. 166, 553–573.
Dalton, C.A., Ekstrom, G., Dziewonski, A.M., 2009. Global seismological shear velocity and attenuation: A comparison with experimental observations. Earth Planet. Sci. Lett. 284, 65–75.
Debayle, E., 1999. Sv-wave azimuthal anisotropy in the Australian upper mantle: Preliminary results from automated waveform inversion. Geophys. J. Int. 137, 747–754.
Debayle, E., Sambridge, M., 2004. Inversion of massive surface wave data sets: Model construction and resolution assessment. J. Geophys. Res. 109, B02316, http://dx.doi.org/10.1029/2003JB002652.
Dziewonski, A.M., Chou, T.-A., Woodhouse, J.H., 1981. Determination of earthquake source parameters from waveform data for studies of global and regional seismicity. J. Geophys. Res. 86, 2825–2852.
Engdahl, E.R., van der Hilst, R., Bulland, R., 1998. Global teleseismic earthquake relocation with improved travel times and procedures for depth determination. Bull. Seismol. Soc. Am. 88, 722–743.
Farver, J.R., Yund, R.A., 2000. Silicon diffusion in forsterite aggregates: Implications for diffusion accommodated creep. Geophys. Res. Lett. 27, 2337–2340.
Faul, U.H., Jackson, I., 2005. The seismological signature of temperature and grain size variations in the upper mantle. Earth Planet. Sci. Lett. 234, 119–134.
Faul, U.H., Jackson, I., 2007. Diffusion creep in dry, melt-free olivine. J. Geophys. Res. 112, B04204, http://dx.doi.org/10.1029/2006JB004586.
Fei, H., et al., 2012. High silicon self-diffusion coefficient in dry forsterite. Earth Planet. Sci. Lett. 345 (8), 95–103.
Goff, J.A., Cochran, J.R., 1996. The Bauer scarp ridge jump: A complex tectonic sequence revealed in satellite altimetry. Earth Planet. Sci. Lett. 14, 21–33.
Goes, S., Govers, R., Vacher, P., 2000. Shallow mantle temperatures under Europe from P and S wave tomography. J. Geophys. Res. 105, 11153–11169.
Gribb, T.T., Cooper, R.F., 1998. Low-frequency shear wave attenuation in polycrystalline olivine: Grain boundary diffusion and the physical significance of the Andrade model for viscoelastic rheology. J. Geophys. Res. 103, 27267–27279.
Gutenberg, B., 1959. Physics of the Earth's Interior. Academic, New York and London.
Hirth, G., Kohlstedt, D., 2003. Rheology of the upper mantle and mantle wedge: A view from experimentalists. In: Inside the Subduction Factory. In: Geophysical Monograph, vol. 138. AGU, pp. 83–105.
Isaack, D.G., 1992. High temperature elasticity of iron-bearing olivines. J. Geophys. Res. 97, 1871–1885.
Jackson, I., 2000. Laboratory measurements of seismic wave dispersion and attenuation: Recent progress. In: The Earth's Deep Interior: Mantle Physics and Tomography from Atomic to the Global Scale. In: Geophysical Monograph, vol. 117. AGU, pp. 265–289.
Janney, P.E., Shirey, S.B., Carlson, R.W., Pearson, D.G., Bell, D.R., Le Roex, A.P., Ishikawa, A., Nixon, P.H., Boyd, F.R., 2010. Age, composition and thermal characteristics of South African off-craton mantle lithosphere: Evidence for a multistage history. J. Petrol. 51, 1849–1890.
Jordan, T.H., 1979. Mineralogies, densities and seismic velocities of garnet lherzolites and their geophysical implications. In: Boyd, F.R., Meyer, H.O.A. (Eds.), The Mantle Sample: Inclusions in Kimberlites and Other Volcanics. AGU, Washington, pp. 1–14.
Karato, S., 2008. Deformation of Earth Materials. Cambridge University Press.
Kojitani, H., Akaogi, M., 1997. Melting enthalpies of mantle peridotite: Calorimetric determinations in the system CaO–MgO–Al_2O_3–SiO_2 and application to magma generation. Earth Planet. Sci. Lett. 153, 209–222.
Kustowski, B., Ekström, G., Dziewoński, A.M., 2008. Anisotropic shear-wave velocity structure of the Earth's mantle: A global model. J. Geophys. Res. 113, B06306, http://dx.doi.org/10.1029/2007JB005169.

Lekić, V., Romanowicz, B., 2011. Inferring upper-mantle structure by full waveform tomography with the spectral element method. Geophys. J. Int. 185, 799–831, http://dx.doi.org/10.1111/j.1365-246X.2011.04969.x.

Li, X., Yuan, X., Kind, R., 2007. The lithosphere–asthenosphere boundary beneath the western United States. Geophys. J. Int. 170, 700–710, http://dx.doi.org/10.1111/j.1365-246X.2007.03428.x.

Lonsdale, P., 2005. Creation of the Cocos and Nazca plates by fission of the Farallon plate. Tectonophysics 404, 237–264.

Malvern, L.E., 1969. Introduction to the Mechanics of a Continuous Medium. Prentice-Hall, New Jersey, USA..

McCarthy, C., Takei, Y., 2011. Anelasticity and viscosity of partially molten rock analogue: Toward seismic detection of small qualities of melt. Geophys. Res. Lett. 38, http://dx.doi.org/10.1029/2011GL048776.

McCarthy, C., Takei, Y., Hiraga, T., 2011. Experimental study of attenuation and dispersion over a broad frequency range: 2. The universal scaling of polycrystalline materials. J. Geophys. Res. 116, B09207, http://dx.doi.org/10.1029/2011JB008384.

McKenzie, D., 2010. The influence of dynamically supported topography on estimates of T_e. Earth Planet. Sci. Lett. 295, 127–138.

McKenzie, D., Priestley, K., 2008. The influence of lithospheric thickness on continental deformation. Lithos 102, 1–11.

Müller, R.D., Sdrolias, M., Gaina, C., Roest, W.R., 2008. Age, spreading rates and spreading symmetry of the world's ocean crust. Geochem. Geophys. Geosyst. 9, Q04006, http://dx.doi.org/10.1029/2007GC001743.

Nataf, H.-C., Ricard, Y., 1996. 3SMAC: An a priori tomographic model of the upper mantle based on geophysical modelling. Phys. Earth Planet. Inter. 95, 101–122.

Nickel, K.G., Green, D.H., 1985. Empirical geothermobarometry for garnet peridotites and implications for the nature of the lithosphere, kimberlites and diamonds. Earth Planet. Sci. Lett. 73, 158–170.

Nimis, P., Grütter, H., 2010. Internally consistent geothermometers for garnet peridotites. Contrib. Mineral. Petrol. 159, 411–427.

Nye, J.F., 1957. Physical Properties of Crystals. Oxford University Press.

Okal, E.A., Bergeal, J.-M., 1983. Mapping the Miocene Farallon Ridge jump on the Pacific plate: A seismic line of weakness. Earth Planet. Sci. Lett. 63, 113–122.

Owen, H.G., 1983. Atlas of Continental Displacement: 200 Million Years to Present. Cambridge University Press.

Panning, M.P., Lekić, V., Romanowicz, B.A., 2010. Importance of crustal corrections in the development of a new global model of radial anisotropy. J. Geophys. Res. 115, B12325, http://dx.doi.org/10.1029/2010JB007520.

Priestley, K., McKenzie, D., 2006. The thermal structure of the lithosphere from shear wave velocities. Earth Planet. Sci. Lett. 244, 285–301.

Priestley, K., McKenzie, D., Debayle, E., Pilidou, S., 2008. The African upper mantle and its relationship to tectonics and surface geology. Geophys. J. Int. 175, 1108–1126, http://dx.doi.org/10.1111/j.1365-246X.2008.03951.x.

Priestley, K., McKenzie, D., Barron, J., Tatar, M., Debayle, M., 2012. The Zagros core: Deformation of the continental lithospheric mantle. Geochem. Geophys. Geosyst. 13, Q11014, http://dx.doi.org/10.1029/2012GC004435.

Ritsema, J., Deuss, A., van Heijst, H.J., Woodhouse, J.H., 2011. S40RTS: A degree-40 shear-velocity model for the mantle from new Rayleigh wave dispersion, teleseismic travel time and normal mode splitting function measurements. Geophys. J. Int. 184, 1223–1236.

Rychert, C.A., Shearer, P.M., 2009. A global view of the lithosphere–asthenosphere boundary. Science 324, 495–498.

Schmerr, N., 2012. The Gutenberg discontinuity: Melt at the lithosphere–asthenosphere boundary. Science 335, 1480–1483.

Schutt, D.L., Lesher, C.E., 2006. Effects of melt depletion on the density and seismic velocity of garnet and spinel lherzolite. J. Geophys. Res. 111, B05401, http://dx.doi.org/10.1029/2003JB002950.

Sieminski, A., Lévêque, J.-J., Debayle, E., 2004. Can finite-frequency effects be accounted for in ray theory surface wave tomography? Geophys. Res. Lett. 31, L24614, http://dx.doi.org/10.1029/2004GL-21402.

Smith, M.L., Dahlen, F.A., 1973. The azimuthal dependence of Love and Rayleigh wave propagation in a slightly anisotropic medium. J. Geophys. Res. 78, 3321–3333.

Taylor, W.R., 1998. An experimental test of some geothermometer and geobarometer formulations for upper mantle peridotites with application to the thermobarometry of fertile lherzolite and garnet websterite. N. Jb Min. Abh. 172, 381–408.

Tommasi, A., 1998. Forward modelling of the development of seismic anisotropy in the upper mantle. Earth Planet. Sci. Lett. 160, 1–13.

Watts, A.B., 2001. Isostasy and Flexure of the Lithosphere. Cambridge University Press, Cambridge, UK.

White, R.S., McKenzie, D., O'Nions, R.K., 1992. Oceanic crustal thickness from seismic measurements and rare earth element inversions. J. Geophys. Res. 97, 19683–19715.

Yuan, H., Romanowicz, B., 2010. Lithospheric layering in the North American Craton. Nature 466, 1063–1068, http://dx.doi.org/10.1038/nature09332.

Zhao, S., Lambeck, K., Lidberg, M., 2012. Lithosphere thickness and mantle viscosity inverted from GPS-derived deformation rates in Fennoscandia. Geophys. J. Int. 190, 278–292.